Smart Materials in Medicine 4 (2023) 199–211

Contents lists available at ScienceDirect

Smart Materials in Medicine

journal homepage: www.keaipublishing.com/en/journals/smart-materials-in-medicine/

A pH/temperature responsive nanocomposite for chemo-photothermal synergistic cancer therapy

Rawand A. Mustafa [a,1], Meixin Ran [a,1], Yonghui Wang [a,1], Jiaqi Yan [a], Yu Zhang [b,***], Jessica M. Rosenholm [a,**], Hongbo Zhang [a,c,*]

[a] Pharmaceutical Sciences Laboratory, Faculty of Science and Engineering, Åbo Akademi University, Turku, 20520, Finland
[b] Department of Pharmaceutics, School of Pharmacy, Shenyang Pharmaceutical University, 103 Wenhua Road, Shenyang, 110016, Liaoning, PR China
[c] Turku Bioscience Centre, University of Turku and Åbo Akademi University, Turku, 20520, Finland

ARTICLE INFO

Keywords:
Gold nanorod
Mesoporous silica
Combined chemo-photothermal therapy
Dual pH/temperature responsive polymer
Drug delivery
Breast cancer

ABSTRACT

To optimize synergistic breast cancer treatment, a nanocomposite was fabricated with pH-temperature responsive and chemo-photothermal combination therapy. Herein, gold nanorods (AuNRs) are coated with [poly[(N-isopropylacrylamide)-co-(methacrylic acid)] (p(NIPAM-co-MAA)) modified mesoporous silica (MS) for Doxorubicin (DOX) delivery (AuNR@DOX-MS@p(NIPAM-co-MAA)). Upon NIR radiation, the AuNR core induced hyperthermia via generating heat. Simultaneously, the polymer layer collapsed in response to high temperature/low pH, which allowed the triggering of DOX release from the MS shell at the tumor site. With this nanocomposite, nearly zero premature release of DOX at physiological pH/temperature was detected, while effective DOX release was reported at higher temperature/lower pH values. In addition, *in vitro* studies demonstrated that the nanocomposite has a substantial uptake efficiency of MDA-MB-231 breast cancer cells, with a significant increase in suppressing MDA-MB-231 cell proliferation in response to laser irradiation. The *in vivo* experiments further verified the high efficiency of the fabricated nanocomposite in accumulating at the tumor site and the good capability in suppressing tumor growth in the mice upon intravenous injection, while exhibiting good biosafety in relation to major organs in the body. Thus, the synthesized nanocomposite could be a potential nanocarrier for breast cancer treatment with synergistic chemo-photothermal therapeutic capability.

1. Introduction

Breast cancer has remained one of the most significant health burdens on global scale, with an estimated 2.3 million new cases (11.7% of all cancer cases) being diagnosed in women every year [1]. The unique physicochemical properties of nanomaterials have recently offered variable opportunities in many diagnostic and therapeutic applications in this regard [2–5]. In particular, nanoparticle-based chemotherapy has gained attention for solving many challenges associated with conventional cancer treatments, such as lack of specificity toward cancer cells or tissues, side effects on normal tissues, and multiple drug resistance [6–13]. Single chemotherapy as a common therapeutic regimen against cancer is associated with the above-mentioned limitations, especially regarding drug resistance, which is considered a major obstacle in successful cancer therapy [14–16]. In addition, delivery of multiple anti-cancer agents in a single dose suffers from subpar pharmacokinetics at the target site. Thus, the systematic combination of cancer treatments with different mechanisms such as chemotherapy, radiotherapy, and photothermal therapy has emerged as an alternative approach to diminish the aforementioned side effects with promising therapeutic efficacy through synergistic actions [7,15,17–19]. Combined chemo-photothermal based nanoparticle combination therapy approach is associated with lower systemic side effects, reduced drug resistance, noninvasive, remote controllability, and improved selectivity [6,9,20–22].

Up to now, several nanomaterial-based near infrared (NIR) photothermal transducers have been reported, such as gold nanostructures, carbon nanotubes, graphene oxide, gold nanocages, gold nanostars, as well

* Corresponding author. Pharmaceutical Sciences Laboratory, Faculty of Science and Engineering, Åbo Akademi University, Turku, 20520, Finland.
** Corresponding author.
*** Corresponding author.
E-mail addresses: pharmzy@163.com (Y. Zhang), Jessica.Rosenholm@abo.fi (J.M. Rosenholm), hongbo.zhang@abo.fi (H. Zhang).
[1] Equal contribution.

https://doi.org/10.1016/j.smaim.2022.09.004
Received 15 July 2022; Received in revised form 7 September 2022; Accepted 18 September 2022
Available online 8 October 2022

as graphene nanosheets [18,23–26]. Among them, AuNRs are considered as an optimum photothermal agent and are therefore broadly applied in photothermal therapy and as drug carriers, due to tunable localized surface plasmon resonance (LSPR) between 750 and 950 nm by modifying their aspect ratio and the easy surface functionalization capability [27–31]. Moreover, AuNRs have a much higher absorption cross section to convert NIR light to heat than gold nanospheres or nanoshells, which leads to ablation of cancer cells directly or triggers drug release when gold nanorods (AuNRs) are used as nanocarriers [32–35]. However, the direct use of AuNRs suffers from some limitations, such as lower biocompatibility due to their stabilization with toxic cetyltrimethylamonium bromide (CTAB) coating, low loading capacity, and shifting of the LSPR peak of gold nanostructures to the visible spectral region as a result of the easy clustering and aggregating of AuNPs upon NIR laser illumination, thus reducing the efficiency of photothermal therapy in the NIR window and delivery of anticancer drugs [5,22,28,36,37]. To overcome these limitations, biomolecules, biopolymers, and mesoporous silica (MS) have been coated on top of AuNRs [24,38–40]. Among them, utilizing MS to coat AuNRs (AuNR@MS) is the most effective approach for AuNR promotion. This is due to the silica shell possessing adequate biocompatibility, large surface area, high loading capacity, enhancing colloidal stability, and facile surface modification possibilities. The AuNR@MS can provide effective synergistic chemo-photothermal therapy as the MS shell can act as a reservoir for molecular chemotherapeutics, while the AuNR core can induce photothermal therapy and trigger drug release as a heat generator [4,7,28,41–43].

In addition, the accumulation of nanocarrier system mediated cancer therapy at the target site is crucial to deliver and induce drug release in a controllable and effective manner, resulting in efficient cancer treatment, lower systemic side effects, and enhanced cellular uptake [9]. To achieve this, the precise spatial (at the target site) and temporal (at the right time) control of the drug-loaded nanocarriers are the main prerequisites for obtaining efficient delivery systems [32,39]. There are many drug release and tumor–targeting approaches that have been reported and relied either on the properties of using stimuli or physiological parameters. For instance, internal stimuli such as pH, temperature, reactive oxygen species (ROS), glucose, antigen, enzyme or thiol-redox responsive materials have been utilized in the design of stimuli-responsive drug delivery systems [8,44–48], while external stimuli that have been utilized for the same include electromagnetic field, ultrasound and light [7,47,49–51]. Another promising approach to controlling release behavior is modifying the surface of the nanocarrier using responsive polymers, organic molecules, and lipid layers [22,24,37,52]. The emergence of multi-responsive polymers has gained wide attention, since it allows to control and trigger drug release efficiently in response to multiple stimuli. Dual pH-thermo responsive materials have been shown to be especially promising in cancer treatment, due to pathological conditions of cancer being present either by an increase in local temperature (2–5°C) or decrease in pH (1 - 2.2 pH units) within the tumor [9,53]. (N-isopropylacrylamide) (NIPAM), poly (N-isopropylacrylamide-co-acrylic acid), and poly (N-isopropylacrylamide-co-N-hydroxymethyl acrylamide) are among the most prominent thermo-responsive polymers that have been widely applied and reported in drug delivery [54–62]. Here, a co-monomer unit (methacrylic acid) is needed to turn the low cloud point temperature (CPT) to above human body temperature (up to 39°C). Thus, under CPT, the thermo-responsive polymer would be expanded and in a hydrophilic state due to the presence of hydrogen bonds, which allows it to retain drug molecules inside the nanocarrier especially at physiological body temperature (37°C). When the temperature is increased above CPT, the copolymer is hydrophobic and can be collapsed to undergo phase transition, leading to the release of the incorporated drug. In addition, the copolymer chain possesses pH responsive properties with the incorporation of methacrylic acid [63,64]. Furthermore, an externally applied NIR laser can trigger drug release at a tumor site [65].

Therefore, we developed a nanocomposite (AuNR@DOX-MS@p(NIPAM-co-MAA)) that could respond to these stimuli and which is shown in Scheme 1, by utilizing dual pH-temperature responsive polymer poly(N-isopropylacrylamide-co-methacrylic acid) (p(NIPAM-co-MAA)) as a gatekeeper on the surface of mesoporous silica coated gold nanorods, which were loaded with Doxorubicin (AuNR@DOX-MS). Upon localized NIR radiation at the tumor site, the AuNR core generated heat increases the ambient temperature of the polymer to exceed CPT, which results in acceleration of DOX release from the porous silica shell acting as a drug reservoir. Since drug release is not triggered at normal physiological conditions, the nanocomposite should exhibit lower toxic side effects at physiologic pH and temperature (7.4 and 37°C) and provide biocompatible and efficacious synergistic chemo-photothermal treatment *in vivo* and *in vitro*.

2. Materials and methods

2.1. Materials

Tetraethyl orthosilicate (TEOS), Ascorbic acid (AA), poly[(N-isopropylacrylamide)-co- (methacrylic acid)] (p(NIPAM-co-MAA)), absolute ethanol and ammonium nitrate (NH_4NO_3) were purchased from Sigma-Aldrich, sodium borohydride ($NaBH_4$), silver nitrate ($AgNO_3$) were purchased from Fluka, cetyltrimethylammonium bromide (CTAB), sodium hydroxide (NAOH), 3-aminopropyltriethoxysilane (APTES) were purchased from Argos, gold (III) chloride trihydrate ($HAuCl_4.3H_2O$) and Doxorubicin were purchased from Macklin Inc. Dulbecco's Modified Eagle Medium (DMEM), penicillin, streptomycin, and L-Glutamine were purchased from Lonza. DMEM/F12 was obtained from Thermo Fisher. The epidermal growth factor (EGF) was purchased from Abcam.

2.2. Methods

2.2.1. Synthesis of AuNRs

The AuNRs were prepared by the seed-mediated growth method according to a published protocol [66] with minor modification. Firstly, the seed solution was prepared by adding 25 μl of 50 mM $HAuCl_4.3H_2O$ into 4.7 ml of 0.1 M CTAB in a 10 ml glass tube and was stirred gently for 2–5 min or more in a 30°C water bath, till it became a clear solution. To this, 300 μl of 10 mM ice-cold $NaBH_4$ was added at once, with vigorous stirring for 1–2 min and kept without shaking at 30°C in a water bath, and the seed solution color changed to light brown immediately.

Second, preparing the growth solution was started by adding 1000 μl of 50 mM HAuCl4.3H2O into 100 ml of 0.1 M CTAB in a glass bottle and gently stirring for 5–10 min in a 30°C water bath to obtain a clear solution. Later to this, by adding 750 μl of 100 mM ascorbic acid (AA) and stirring gently for a few seconds, the solution became colorless. After that, 800 μl of 5 mM $AgNO_3$ solution was added and stirred gently for a few more seconds. Finally, 120 μl of prepared seed solution was added into the growth solution and stirred gently for 10–20 s to mix the whole mixture properly, and then incubated for 24 h in a 30°C water bath without shaking. The color of the solution was gradually changed to a purple color. After a 24-h incubation, the prepared AuNR was centrifuged once at 16000 rpm for 20 min at 18°C, then washed once with deionized water and centrifuged at the same parameters to remove unreacted CTAB and other impurities. Finally, the obtained AuNR was re-dispersed in 10 ml of deionized water and stored at +4°C for further use.

2.2.2. Synthesis of AuNR@MS

The core-shell (AuNR@MS) particles were prepared by coating the AuNR core with a porous silica layer using the Stöber method. The synthesis depends on the hydrolysis of TEOS under alkaline conditions, in the presence of AuNR as seed and CTAB as soft template [18,22,42]. First, 10 ml of as-prepared AuNR suspension was adjusted to pH 10–11 with the aid of 0.1 M NaOH, followed by transfer into a round bottom flask and starting stirring at 300 rpm in a 30°C water bath for 20 min to equilibrate the suspension temperature. Afterwards, the reaction was started by adding 120 μl of freshly prepared (20% TEOS in absolute

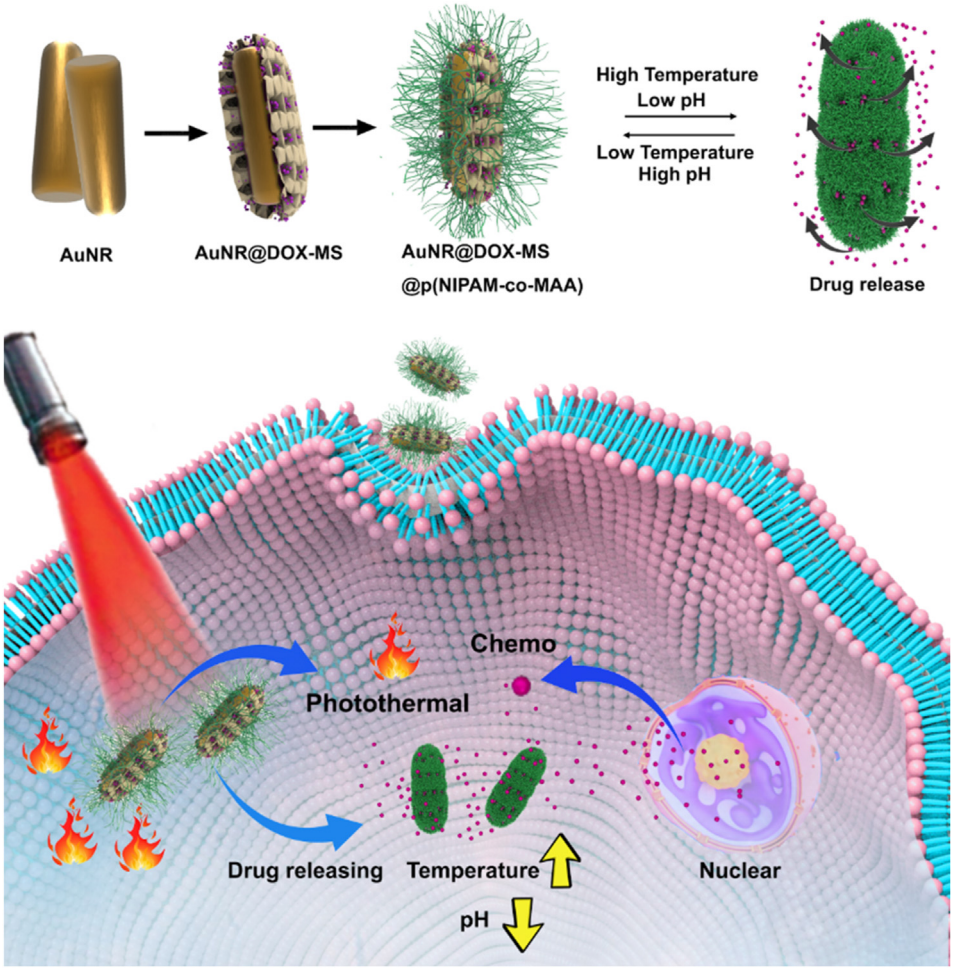

Scheme 1. Schematic diagram of the synthesized nanocomposite (AuNR@DOX-MS@p(NIPAM-co-MAA)) and envisioned drug release inside the cell.

ethanol) step-wise (within 10–15 min) under stirring, and the reaction was continued for 24 h. After 24 h, the obtained AuNR@MS was centrifuged at 16000 rpm, 18°C for 20 min. Then, it was re-dispersed in 30 ml of NH_4NO_3 ethanol solution (1% wt) and kept under vigorous stirring for 6 h twice in a 30°C water bath to remove excess CTAB and unreacted silica. Later, the prepared AuNR@MS was washed with absolute ethanol and centrifuged at the same speed to remove extra NH_4NO_3. Finally, the AuNR@MS was re-dispersed in absolute ethanol and kept at +4°C for further use.

2.2.3. Synthesis of AuNR@MS-NH_2

The surface modification of synthesized AuNR@MS was performed by using 3-aminopropyltriethoxysilane to add primary NH_2 groups onto the silica layer. 100 mg of synthesized AuNR@MS was dispersed in 20 ml of absolute ethanol and incubated in a 30°C water bath under stirring with 200 μl of 3-aminopropyltriethoxysilane. After 24 h of refluxing, the AuNR@MS-NH_2 was collected and washed twice with absolute ethanol to remove unreacted 3-aminopropyltriethoxysilane by using centrifugation at 16000 rpm, 20 min, and 18°C temperature [67].

2.2.4. DOX loading in AuNR@MS

Doxorubicin loading into AuNR@MS was carried out using the solvent immersion method. 3 mg of DOX (3 mg/ml as optimal concentration, see Supplementary Material Table S1) was dissolved in PBS solution (pH 7.4) under sonication, followed by suspending 1 mg of AuNR@MS in DOX solution using sonication for 20 min. Then, the suspension was put in a rotating wheel for 24 h at 60 rpm, room temperature, and in the dark. The AuNR@DOX-MS was collected using centrifugation at 13500 rpm at room temperature for 10 min, followed by washing with PBS twice. The amount of DOX in the supernatant was determined using a Thermo Fisher Scientific 2000c UV–Vis spectrophotometer at 480 nm to calculate the drug loading content. The loading efficiency (LE%) and loading content (LC%) of DOX were calculated according to the following Equations (1) and (2): [39].

$$LE\% = \text{total amount of input DOX} - \text{free DOX in supernatant/ total amount of input DOX} \times 100 \quad (1)$$

$$LC\% = \text{entrapped DOX/ weight of nanoparticle} \times 100 \quad (2)$$

2.2.5. Synthesis AuNR@DOX-MS@p(NIPAM-co-MAA)

The surface coating of AuNR@DOX-MS was performed by physical adsorption in p(NIPAM-co-MAA) solution. Briefly, 1 mg of AuNR@DOX-MS was dispersed in p(NIPAM-co-MAA)) solution (2mg/ml ethanol) in a sonication bath for few minutes. Then, the mixed suspension was continued on stirring for 24 h at room temperature. The obtained AuNR@DOX-MS@p(NIPAM-co-MAA) was collected by centrifugation at 16000 rpm, 20 min and 18°C temp, and washed twice with ethanol to remove unreacted p(NIPAM-co-MAA)) and freeze-dried [68].

2.2.6. Photothermal measurement of AuNR@DOX-MS@p(NIPAM-co-MAA)

The photothermal efficacy of AuNR@DOX-MS@p(NIPAM-co-MAA) was evaluated by carrying out three experiments as follow: first, concentration-dependent photothermal measurements were done by

placing 1 ml of aqueous dispersion of AuNR@DOX-MS@p(NIPAM-co-MAA) with different concentrations (0.1, 0.5,1,1.5 and 2 mg/ml) in a tube and irradiated with NIR laser (808 nm, 2 W cm^{-2}, 300 s) and the thermal imaging pictures were immediately recorded every 30 s by a thermal imaging camera. Second, laser power density-dependent photothermal measurements were conducted by introducing 1 ml of aqueous dispersion of AuNR@DOX-MS@p(NIPAM-co-MAA) with the same concentration (1.5 mg/ml) to a tube and irradiated with a NIR laser at different power densities (0.5, 1.0, 1.5 and 2 W cm^{-2}, 300 s) respectively. Third, heating-cooling cycles experiments were performed with the aid of using 1 ml of AuNR@DOX-MS@p(NIPAM-co-MAA) (1mg/ml) suspension and continually irradiated by a NIR laser at (808 nm, 1 W cm^{-2}) to reach the plateau temperature. Then it was cooled down naturally to room temperature. The changing of temperature and thermal images were simultaneously recorded and taken every 30 s by a digital thermometer camera in all three conducted experiments [32,39].

2.2.7. In vitro triggered drug release via NIR

An *in vitro* drug release experiment was carried out at different pH (7.4 and 5) of phosphate buffer saline (PBS) media and body temperature (37°C) to simulate physiological and cancer microenvironment pH/temp. At each predetermined time point, 1 ml of dispersed AuNR@DOX-MS@p(NIPAM-co-MAA) in PBS (1 mg/ml) was agitated in a shaker bath at (37°C) and pH (7.4 and 5). The amount of released drug in the supernatant was collected at a predetermined time by centrifugation and measured by a UV–Vis spectrometer at 480 nm. The same method was applied in the NIR laser-controlled drug release experiments. At a determined time interval, 1 ml of dispersed AuNR@DOX-MS@p(NIPAM-co-MAA) in PBS (1 mg/ml) was irradiated with a NIR laser at (808 nm, 1 W cm^{-2}, 5 min) at pH (7.4 and 5) [22].

2.2.8. Characterization

The morphology, size, and aspect ratio of nanoparticles were studied with the aid of the JEM-1400 Plus TEM by placing 5 μl of dispersed nanoparticles in either ethanol or aqueous solution on carbon-coated copper grids (200 mesh; Ted Pella, Inc., U.S.A.), and allowing them to dry in air before imaging. The zeta potential, hydrodynamic size, and PDI of nanoparticles were examined using the Malvern Zeta Sizer ZS (PCS, Malvern Instruments Ltd). In addition, to study the surface structure of drug, polymer and synthesized nanocomposite with different surface modifications, FTIR spectra were measured using PerkinElmer Spectrum Two, scanning from 4,000 to 400 cm^{-1}. The optical properties of synthesized AuNR with different surface modifications were measured by the Themo Fisher Scientific 2000c UV–Vis spectrophotometer using a 1-cm-wide quartz cuvette.

2.2.9. Cell study

2.2.9.1. Cell culture and maintenance. MDA-MB231 triple-negative breast cancer cells were cultivated in DMEM media supplemented with 10% FBS and 1% penicillin, streptomycin at 37°C, while MCF-10A healthy cells were grown in Eagle's Minimum Essential Medium (DMEM/F12) supplemented with 1% penicillin, streptomycin, and epidermal growth factor EGF (20 ng/ml final concentration in medium) and 2 mM L-glutamine in a humidified incubator with 5% CO_2. All cell lines were passed when their densities reached approximately 90%.

2.2.9.2. Cytotoxicity assay. A WST-1 cell viability assay was used to determine the cytocompatibility of drug and synthesized nanocomposite AuNR@DOX-MS@p(NIPAM-co-MAA) in healthy (MCF-10A) and cancerous (MDA-MB-231) cells lines. MCF-10A and MDA-MB-231 cells were plated in a 96-well microplate at a high density (5000 cells per well) and incubated for 24 h at 37°C. The experiment was divided into 7 groups during cell incubation: DOX, AuNR@MS-Laser, AuNR@MS + Laser, AuNR@DOX-MS-Laser, AuNR@DOX-MS + Laser, AuNR@DOX-MS@p(NIPAM-co-MAA)-Laser and AuNR@DOX-MS@p(NIPAM-co-MAA)+Laser groups. Each group had a 0, 0.1, 1, 2, 4, 6, 8 and 10 μg/mL DOX equivalent concentration. After 24 h of incubation, the cell media was replaced with fresh media containing free drug or other groups as mentioned with different concentrations and incubated for another 24 h. Among them, the +Laser group was irradiated at (808 nm, 1 W cm^{-2}, 5 min) after 24 h of incubation. Later, 10 μL of WST-1 solution were added to each well and incubated for 4 h in the cell culture incubator (37°C, 5% $CO_{2)}$. Finally, the absorbance was measured at 450 nm by a Varioskan Flash Multimode Reader (Thermo Scientific Inc., Waltham, MA, USA) at 440 nm [5,69].

2.2.9.3. Intracellular uptake study by flow cytometry. Flow cytometry was used to study the uptake efficiency of nanocomposite AuNR@DOX-MS@p(NIPAM-co-MAA) in healthy (MCF-10A) and breast cancer (MDA-MB-231) cell lines. Cells were grown on confocal dishes (1×10^5 cells per well cell per dish) in a 6-well plate overnight. The next day, the cell media was replaced, and the cells were exposed to new media containing AuNR@DOX-MS and AuNR@DOX-MS@p(NIPAM-co-MAA) groups. Each group with 4 μg/mL DOX equivalent concentration, after 2 h and 4 h time points of incubation, the cells were rinsed with PBS twice, collected the cells and tested under flow cytometry.

2.2.9.4. Cell apoptosis by flow cytometry. A flow cytometry method was utilized to quantify intracellular uptake of DOX with a flow based on the spontaneous fluorescence property of DOX. Cells were seeded in the 6 well plates (1×10^5 cells per well) and incubated overnight. Then, the cell media was substituted with fresh media containing DOX, AuNR@MS-Laser, AuNR@MS + Laser, AuNR@DOX-MS-Laser, AuNR@DOX-MS + Laser, AuNR@DOX-MS@p(NIPAM-co-MAA)-Laser and AuNR@DOX-MS@p(NIPAM-co-MAA)+Laser groups with 4 μg/mL DOX equivalent concentration in each group. The laser group was treated as shown in 2.2.9.2. The cell incubation was done at 37°C overnight and was collected. Subsequently, the cells were gently resuspended with PBS and counted. 50,000–100,000 resuspended cells were taken and centrifuged at 1000 g for 5 min. To gently resuspended the cells, 195 μL Annexin V-FITC binding solution was added. 5 μL and 10 μL propidium iodide staining solution Annexin V-FITC was then add and mixed gently. After incubating for 10–20 min at room temperature (20–25°C) in the dark, the cell is then placed in an ice bath. The cellular uptake quantification was measured by the flow cytometer BD LSRFortessa (BD Biosciences) with the aid of using the PE channel (Exmax 496 nm/Emmax 578 nm). All measurements were carried out in triplicate, and the results were analyzed by flow software 2.0. The gate was defined for live cells only; 10,000 cells were recorded per sample. The fluorescence intensities of stocks (drugs and nanoparticles) were measured by a Thermo Fisher Varioskan plate reader for the same Ex/Em values and the results were normalized for comparison of cellular uptake [70,71].

2.2.10. Animal study

An animal study was conducted in compliance with protocol and was approved by the Animal Research Committe of Ruijin Hospital, Shanghai Jiao Tong University School of Medicine, China. The MNNG/HOS tumor-bearing mice were prepared by culturing around 40 bottles of MDA-MB-231 in the cell culture bottle (1×10^7 cells per bottle). After sufficient cell growth, the dilution of each bottle of cells (1×10^7 cells) was done with 100 μL cell medium and injected subcutaneously into the axilla of BALB/c-nu nude mice. The average age of all female nude mice was 6 weeks old. Then all the mice were weighed and evenly divided into four groups according to their weight for the anti-tumor efficacy test. The tumor volume and mass were monitored and recorded every day. The drug or nanocomposite formulation was administrated via tail vein injection (IV). Upon the tumor volume reached about 100 mm^3, mice were divided into four groups including PBS, DOX, AuNR@DOX-MS@p(NIPAM-co-MAA)+Laser, and AuNR@DOX-MS@p(NIPAM-co-MAA)-Laser, each

group including four mice. The *in vivo* experiments included *in vivo* thermo-imaging, *ex vivo* fluorescence imaging, *in vivo* anticancer efficacy, and H & E staining [39,70].

2.2.10.1. Imaging in vivo. To perform an *in vivo* NIR thermograph, the nude mice were anesthetized and placed on the test bench to expose the tumor site. Then the tumor site was irradiated with a laser at (808 nm, 1 W cm^{-2}, 2 min). Simultaneously, thermal images and temperatures were taken and recorded every 30 s using a thermal imaging camera.

2.2.10.2. Ex vivo fluorescence imaging. This experiment was carried out by intravenously administering only one dose of PBS, DOX, AuNR@DOX-MS@p(NIPAM-co-MAA)+Laser, and AuNR@DOX-MS@p(NIPAM-co-MAA)-Laser into nude mice via the tail vein. After 3 days, the mice were sacrificed, and the heart, liver, spleen, lung, kidney, and tumor were collected for *in vitro* fluorescence detection with the aid of using *In-Vivo* MS FX PRO system (Bruker) and histopathological examination.

2.2.10.3. In vivo anticancer efficacy. To evaluate free drug and synthesized nanocomposite tumor efficacy, one dose of PBS, DOX, AuNR@DOX-MS@p(NIPAM-co-MAA)+Laser, and AuNR@DOX-MS@p(NIPAM-co-MAA)-Laser was injected intravenously into nude mice via the tail vein. The DOX concentration in all formulations was equally the same and calculated at 5 mg/kg. Upon the tumor disappearing, the tumor was extracted and photographed along with a calculation of the tumor inhibition rate and weight change. The tumor volumes were calculated using the following equation: $V = (\text{length} \times \text{width}^2)/2$ (3). Tumor inhibition rate (IR) was calculated based on the formula: IR (%) = (1 – TWt/TWc) x 100 (4), where TWt and TWc are the mean tumor weight of treated and controlled groups [18,70].

2.2.10.4. Histopathology. A histopathological test was conducted according to standard procedure. The histopathological examination was done by randomly selecting one mouse and scarifying it. The tumors and organs, including the heart, liver, spleen, lung, and kidney were fixed with fixative for more than 24 h. Then it was placed in a fume hood and trimmed the tissue samples at the target site by using a scalpel. This is followed by dehydration of the tissue with a gradient concentration of alcohol (75% alcohol 4h; 85% alcohol 2h; 90% alcohol 2h; 95% alcohol 1h; anhydrous ethanol 30 min; alcohol benzene 5–10 min; xylene 10 min; 65°C Melting Paraffin 1h). Subsequently, the tissue samples were embedded in paraffin blocks and sectioned into 4 μm slices. The slices were observed, and images were taken using an optical microscope (magnification: liver, heart, spleen, lung, and kidney × 100). Then, the section was stained with hematoxylin staining solution for 3–5 min. A washing procedure was done with tap water and differentiated with a differentiation solution. Later, the sections were dehydrated with 85% and 95% gradient alcohol for 5 min and stained with eosin staining solution for 5 min. Finally, after dehydration and mounting on glass slides, the microscopic examination, image acquisition, and analysis of sections were obtained, in which the nucleus is blue and the cytoplasm is red [39, 70].

2.2.11. Statistical data analysis

All of the data was gathered from separate experiments that were performed in triplicate. All statistical analyses were carried out using the GraphPad prism 9 software and SPSS 20.0 Software (IBM Inc., Armonk, NY, USA). Statistical differences were analyzed by student's t-test and two-way ANOVA. Data are expressed as mean ± SD values. Statistically significant differences were defined as * P <0.05, **P <0.01, ***P <0.001, and ****P <0.0001.

3. Results and discussion

3.1. Synthesis and characterization of AuNR@DOX-MS@p(NIPAM-co-MAA)

To simultaneously deliver chemo-photothermal therapeutic agents into the tumor site and to control and enhance the drug release, the nanocomposite AuNR@DOX-MS@p(NIPAM-co-MAA) has been synthesized. Herein, poly[(N-isopropylacrylamide)-co-(methacrylic acid)] as a pH/temperature responsive polymer was used as surface modification of

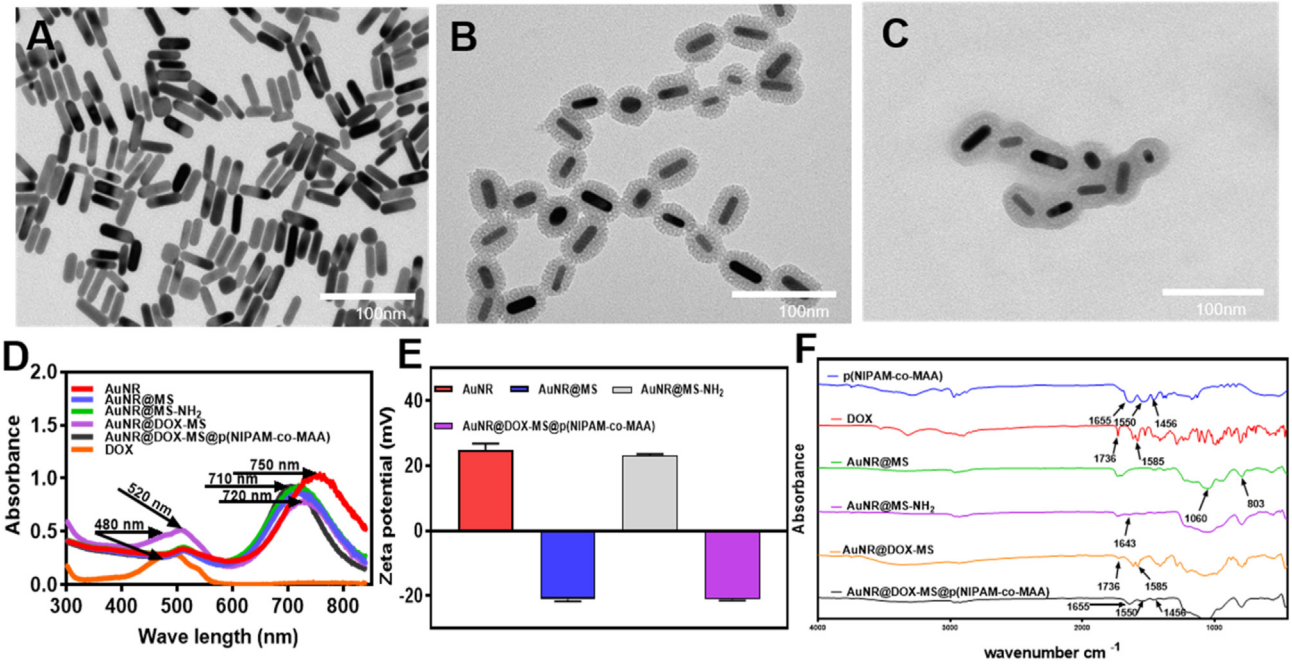

Fig. 1. Characterization of nanoparticle morphology and UV–Vis spectra. TEM images (scale bar. 100 nm) of (A) AuNR, (B) AuNR@MS, and (C) nanocomposite (AuNR@DOX-MS@p(NIPAM-co-MAA)). (D) UV–Vis spectra of DOX, AuNR, AuNR@MS, AuNR@MS-NH_2, AuNR@DOX-MS, and AuNR@DOX-MS@ p(NIPAM-co-MAA). (E) Zeta potential of AuNR, AuNR@MS, AuNR@MS-NH_2, and AuNR@DOX-MS@p(NIPAM-co-MAA). (F) FTIR spectra of p(NIPAM-co-MAA), DOX, AuNR@MS, AuNR@MS-NH_2, AuNR@DOX-MS, and AuNR@DOX-MS@p(NIPAM-co-MAA).

mesoporous silica coated AuNR loaded with DOX as shown in Scheme 1.

First, AuNR with a rod-like shape was synthesized according to a previously published protocol with minor modification [66]. As shown in the TEM image in Fig. 1A, the prepared well-dispersed AuNR had an average length and width of about 38 ± 2 nm and 10 ± 1 nm respectively, with an aspect ratio of 4:1. Then, as shown in Fig. 1B, an MS layer with a uniform thickness of around 12 nm was deposited onto the surface of the AuNR. The MS shell can improve the colloidal stability of AuNR and therefore enhance the transmittance of NIR radiation to biological tissue [18,52]. Furthermore, the synthesized AuNR@MS was further coated with a dual responsive polymer layer by physical adsorption to obtain the hybrid nanocomposite (AuNR@DOX-MS@p(NIPAM-co-MAA)) as described in Scheme 1. As exhibited in Fig. 1C, a thin polymer layer is clearly observed, while the silica pores disappear from the surface as a result of a successful coating with the polymer layer. The UV–Vis spectra is presented in Fig. 1D. AuNR has two absorption peaks; a weak transverse peak at 520 nm and a longitudinal peak at 750 nm [32]. In addition, after coating AuNR with MS shell, there was a small red shift of the longitudinal peak to 720 nm. Moreover, the red shift remained the same in AuNR@MS-NH_2 and AuNR@DOX-MS, while in AuNR@DOX-MS, a small peak was raised at 480 nm, which was assigned to DOX [42,52]. However, an additional red shift was observed for the synthesized nanocomposite (AuNR@-DOX-MS@p(NIPAM-co-MAA)), which could be attributed to the local refractive index in the solution, but the peak was still present in the NIR window [5,33,41,43]. Even though dynamic light scattering (DLS) is not as accurate as other methods for measuring non-isotropic particles such as rod-shaped nanoparticles [72,73], the DLS results as shown in Supplementary Material Fig. S1A and B revealed that the hydrodynamic size of synthesized AuNR@MS and AuNR@DOX-MS@p(NIPAM-co-MAA) was 156 ± 2 and 191 ± 7 respectively, whereas PDI result Fig. S1B showed that the AuNR@MS and AuNR@DOX-MS@p(NIPAM-co-MAA) had homogeneous dispersion. In addition, the narrow size distribution peak can be seen inFig. S2A and B validates the monodispersity of synthesized AuNR@MS and AuNR@DOX-MS@p(NIPAM-co-MAA). The correlation coefficient result in Fig. S3A and B demonstrated that the data quality of size distribution is good as there was no aggregation or precipitation, confirming that the size distribution quality is more reliable. Furthermore, zeta potential measurements for the synthesized nanocomposite AuNR@DOX-MS@p(NIPAM-co-MAA) were carried out to demonstrate that the nanocomposite was successfully formulated. In Fig. 1E, the AuNR core had a positive ζ-potential value due to the presence of CTAB on the surface (+24.9 ± 1.5 mV), and possessed a highly negative ζ-potential when encapsulated in a silica shell AuNR@MS (-20.2 ± 0.4 mV), which was attributed to the formation of abundant Si–OH [22]. Furthermore, the ζ-potential of AuNR@MS was dramatically shifted to positive after being modified with –NH_2 (+23.1 ± 0.3 mV) and finally possessed a highly negative ζ-potential after being coated with the polymer layer (-21.1 ± 0.3 mV), resulting in the formation of a nanocomposite AuNR @DOX-MS@p(NIPAM-co-MAA) as a final formulation. In addition, the formation of AuNR@DOX-MS@p(NIPAM-co-MAA) was further confirmed by conducting FTIR measurement. As exhibited in Fig. 1F, the FTIR characteristic band of AuNR@MS at 1060 cm^{-1} and 803 cm^{-1} was represented by bending vibration Si–O and Si–O–Si stretching vibration, which illustrates a successful coating of the AuNR core by silica shell, while a new vibrational band of amine group N–H at 1643 cm^{-1} appeared, which confirmed successful functionalization of the silica shell surface by-NH_2. Furthermore, the most prominent absorption peak of DOX appeared at 1736 cm^{-1} and 1585 cm^{-1}, which is attributed to carbonyl group stretching bands C═O and C═C respectively, and it appeared even after its loading into AuNR@MS at (AuNR@DOX-MS) [74,75]. The characterization vibration band of polymer p(NIPAM-co-MAA) was observed at 1655 $cm^{-1}$and 1550 cm^{-1}, which belonged to the secondary amide C═O stretching and N–H bending vibrations, respectively. In addition, the IR band at 1456 cm^{-1} represented the bending vibration of C–H [76,77]. FTIR results confirmed that the polymer was successfully coated with AuNR@DOX-MS and hence formulated AuNR@DOX-MS@p(NIPAM-co-MAA).

3.2. Thermoresponsive properties of AuNR@DOX-MS@p(NIPAM-co-MAA)

The photothermal efficacy of fabricated nanocomposite (AuNR@-DOX-MS@p(NIPAM-co-MAA)) was studied as presented in Fig. 2A, B, and C. Different concentrations (0.1, 0.5,1,1.5 and 2 mg ml^{-1}) of AuNR@DOX-MS@p(NIPAM-co-MAA) was irradiated with NIR laser (808 nm, 2 W cm^{-2}, 300 s), and 1.5 mg ml^{-1} of AuNR@DOX-MS@p(NIPAM-co-MAA) was irradiated with NIR laser at different power density (0.5, 1.0, 1.5 and 2 W cm^{-2}) respectively for 300 s. As presented in Fig. 2A and B, the rise in temperature and the intensity of thermal imaging were associated with an increasing concentration of nanocomposite. In particular, irradiating 2 mg ml^{-1} of AuNR@DOX-MS@p(NIPAM-co-MAA) for 300 s resulted in an increased temperature by about 74°C, while the NIR irradiation at the same density did not induce any temperature change in pure water as a control group [18]. Similarly, the temperature increase rate and final temperature were proportionally correlated to the laser power intensity. With increasing power intensity, the temperature of AuNR @DOX-MS@p(NIPAM-co-MAA) increased more significantly, as exhibited in Fig. 2C [32,39]. The presented results demonstrated that the rise in temperature was attributed to the photothermal effect of AuNR.

Moreover, the photostability and photothermal conversion efficiency of the synthesized nanocomposite AuNR@DOX-MS@p(NIPAM-co-MAA) were investigated as a significant characteristic for a successful drug delivery carrier by performing three heating-cooling cycles (Fig. 2D). As illustrated in Fig. 2D, no decrease in the temperature elevation of the nanocomposite was detected after three repeated laser on–off cycles. The temperature of the nanocomposite was increased rapidly and reached a plateau after every cycle of laser irradiation. The photothermal conversion efficiency of AuNR@DOX-MS@ p(NIPAM-co-MAA) was determined as 25% from the heating–cooling curves as seen in Fig. 2D and Supplementary Material Fig. S4. The (η) was obtained using Equations (1) and (2) as follows:

$$\eta = hs\ \Delta T_{max} - Q/\ I\ (1\text{-}10^{-A780}) \quad (1)$$

In this equation, ΔTmax represents the highest value of temperature change, Q denotes the heat rise of the solvent, and I indicates the laser's power. A780 represents the absorbance of the AuNR@DOX-MS@p(NIPAM-co-MAA) at a wavelength of 780 nm, whereas hs can be determined using the following equation:

$$hs = mc/\ \tau \quad (2)$$

The specific heat capacity and mass of the solution are depicted by the letters m and c. τ is the slope of the fitted line from τ to -ln $\Delta T/\Delta T_{max}$ [40, 70]. Furthermore, to confirm the effect of the p(NIPAM-co-MAA) polymer layer on DOX release from AuNR@DOX-MS@p(NIPAM-co-MAA), an *in vitro* release profile study was carried out (Fig. 2E). DOX was loaded into AuNR@MS in PBS buffer at pH 7.4 through electrostatic attraction to form AuNR@DOX-MS. Using a variety of ratios of DOX to AuNR@MS as shown in the Supplementary Material Table S1. The DOX loading content at an optimal ratio with regard to nanoparticle (1:3; AuNR@MS:DOX) was utilized and the loading degree reached up to 26% as quantified by using a UV–Vis spectrophotometer after coating. The release study of DOX was performed at pH 5 and pH 7.4 at 37°C. As presented in Fig. 2E, the DOX cumulative release profile of nanocomposite AuNR @DOX-MS@p(NIPAM-co-MAA) at pH 7.4 without laser and with laser irradiation was 9% ± 3 and 35% ± 2 respectively within 72 h, while the DOX cumulative release increased significantly to 65% ± 4 and 88% ± 3 at pH 5 without laser and after irradiation and heating up the AuNR@DOX-MS@p(NIPAM-co-MAA) with NIR laser at 808 nm, 1 W cm^{-2} for 5 min. As shown in Fig. 2E, a less than 10% DOX cumulative release at physiological pH 7.4 and at normal body temperature 37°C can be observed, owing to the extension of the polymer chain and the CPT of

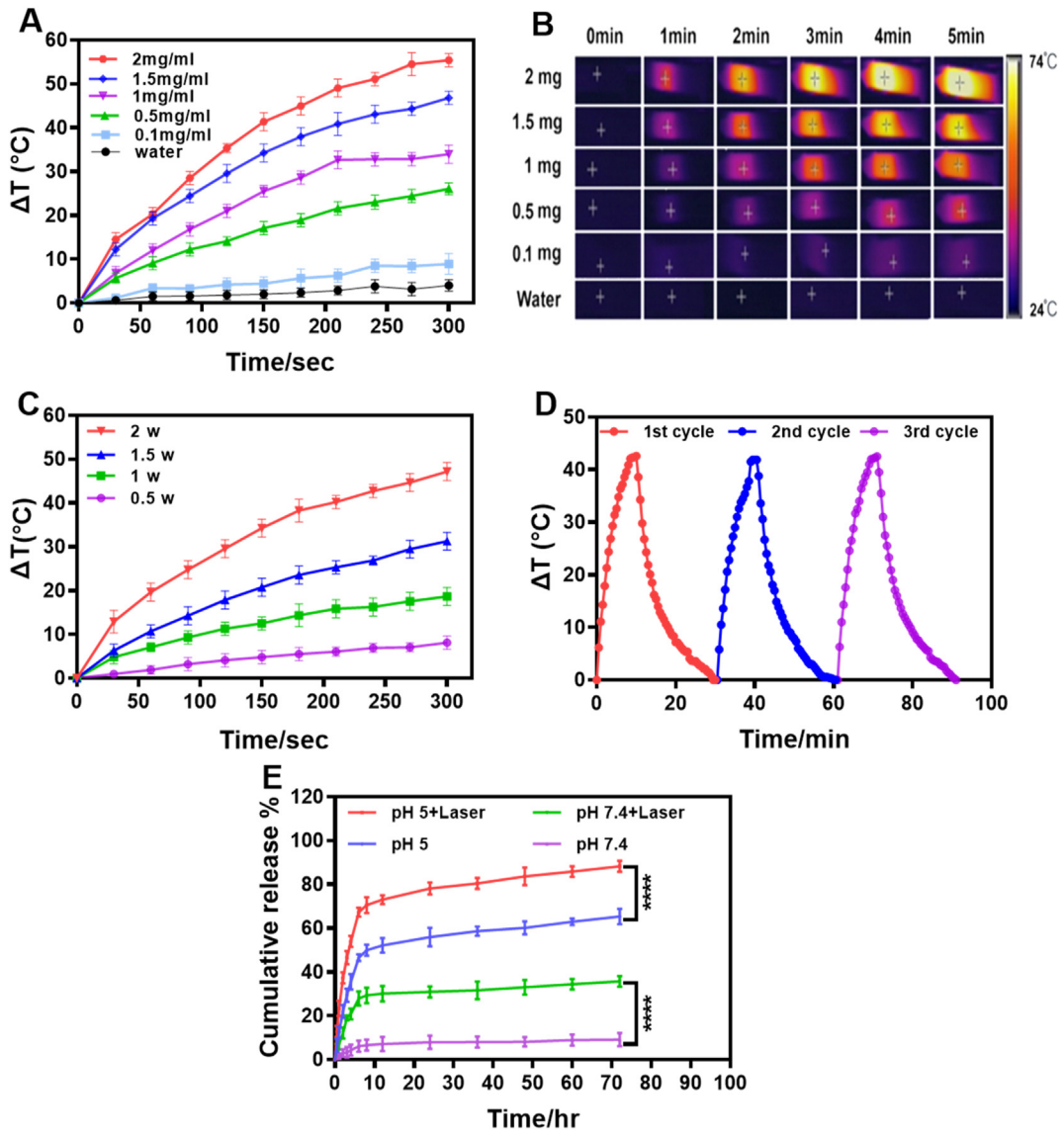

Fig. 2. Photothermal effect characterization and cumulative DOX release profile of synthesized nanocomposite (AuNR@DOX-MS@p(NIPAM-co-MAA)). (A) Photothermal heating curves of DI water and synthesized nanocomposite (AuNR@DOX-MS@p(NIPAM-co-MAA)) with different concentrations (0.1, 0.5, 1, 1.5 and 2 mg mL^{-1}) under 2.0 W cm^{-2}, 808 nm laser irradiation for 0–300 s, and water was used as a control group. (B) The infrared thermal images of DI water and nanocomposite with different concentrations under 2.0 W cm^{-2}, 808 nm laser irradiation for 0–300 s. (C) Photothermal heating curves of 1.5 mg mL^{-1} synthesized nanocomposite was irradiated under different laser powers density (0.5, 1, 1.5 and 2 W/cm^2) for 0–300 s. (D) Temperature elevation of synthesized nanocomposite (1 mg mL^{-1}) over three times of NIR on−off irradiated cycles (1.0 W cm^{-2}, 808 nm). (E) DOX release profile of synthesized nanocomposite (AuNR@DOX-MS@p(NIPAM-co-MAA)) under different condition (n = 3, ****P <0.0001).

the polymer being above body temperature. Thus, the polymer layer could retain the DOX inside the silica pores and prevent it from being released prematurely into healthy tissues [64]. However, DOX cumulative release percentage became significantly higher at pH 5 and further increased under NIR irradiation. This was attributed to the fact that AuNR@DOX-MS@p(NIPAM-co-MAA) is pH/temperature responsive. At pH 5 with NIR laser irradiation at (808 nm, 1 W cm^{-2}, 5 min), the polymer layer collapsed and allowed DOX to release from MS pores, due to decrease in the CPT of p(NIPAM-co-MAA) in an acidic environment and above body temperature. The surface silanol of the mesoporous shell could also be protonated by light NIR-heat and at acidic pH. This led to the weakening of the electrostatic attraction between DOX and the silica surface [5,22,64]. The release study indicated that the synthesized nanocomposite (AuNR@DOX-MS@p(NIPAM-co-MAA) exhibited controlled and enhanced drug release at the tumor site compared with the group without laser and neutral pH.

3.3. AuNR@DOX-MS@p(NIPAM-co-MAA) cytotoxicity and cell apoptosis

In this study, as shown in Fig. 3, the WST-1 assay was used to evaluate the cell proliferation inhibitory potential of the AuNR@DOX-MS@p(NIPAM-co-MAA) nanocomposite in MCF-10A and MDA-MB-231 cell lines. As shown in Fig. 3A, although all the groups exhibited concentration-dependent cytotoxicity, only the highest concentration of AuNR@MS NPs was able to generate some inhibitory effects on the growth of healthy cells (MCF-10A) and cancer cells (MDA-MB-231), demonstrating that the Au@MS NPs were only mildly or non-cytotoxic within the concentration range studied (10 μg/mL) [22,78]. According to the findings of a study conducted on the MCF-10A cell line (Fig. 3A), at a relatively high concentration of 10 μg/ml, MCF-10A cells treated with the AuNR@DOX-MS@p(NIPAM-co-MAA) nanocomposite had considerably higher proliferation abilities than cells treated alone with pure DOX or

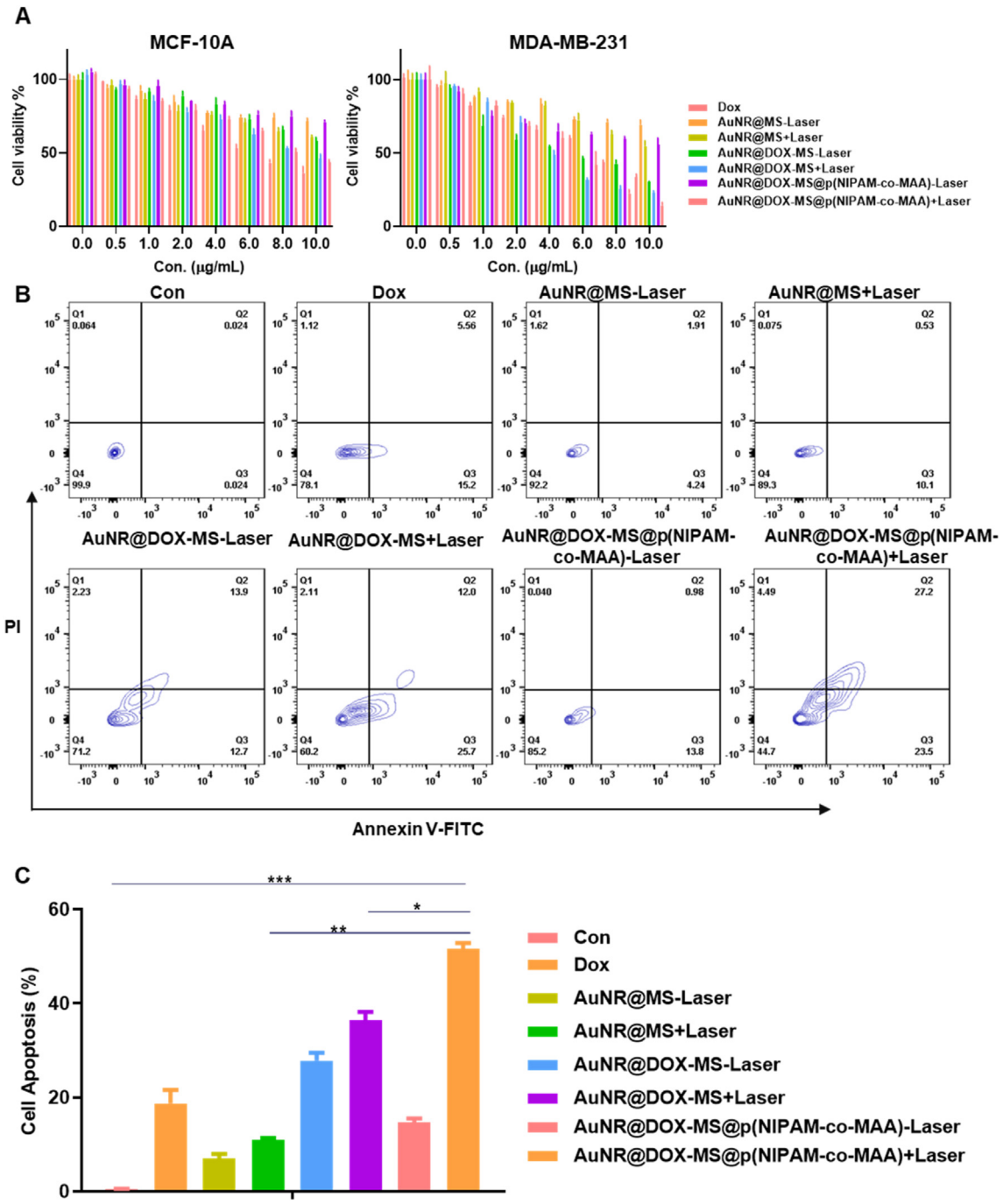

Fig. 3. (A) In vitro cell viability of MCF-10A and MDA-MB-231cell line respectively after treatment with DOX, AuNR@MSN, AuNR@DOX-MS, and AuNR@DOX-MS@p(NIPAM-co-MAA) for 24 h and laser group was treated with NIR laser at (808 nm, 1 W cm^{-2}, 5 min). (B) Flow cytometric apoptosis analysis of MDA-MB-231 tumor cell line under Annexin V-FITC/PI stained. (C) Statistical analysis of MDA-MB-231cells by flow cytometric apoptosis after treatment with DOX, AuNR@MSN, AuNR@DOX-MS, and AuNR@DOX-MS@p(NIPAM-co-MAA) for 24 h and laser group was treated with NIR laser at (808 nm, 1 W cm^{-2}, 5 min) (n = 3, *P <0.05, **P <0.01, and ***P <0.001).

AuNR@DOX-MS, when not exposed to irradiation of laser light, while MCF-10A viability was decreased to less than 50% after treating with AuNR@DOX-MS@p(NIPAM-co-MAA) laser irradiation, which is reasonable, since only cancer cells are exposed to laser irradiation, not healthy cells [39]. In addition, the results obtained in the MDA-MB-231 cell line (Fig. 3A) demonstrated that the laser induction group of AuNR@DOX-MS@p(NIPAM-co MAA) possesses much stronger cell proliferation inhibition compared to the non-exposure group, whereas the laser exposer group of AuNR@DOX-MS and AuNR@MS showed no significant difference in cell proliferation inhibition compared with non-exposure group, this can be concluded that the laser itself has not ability to kill cancer cell in short time and also uncontrollable release behavior of DOX from AuNR@MS without polymer layer [5,15]. Furthermore, the AuNR@DOX-MS@p(NIPAM-co-MAA)+Laser group was shown to be more effective in inhibiting the growth of tumor cells than the AuNR@DOX-MS groups and pure DOX. This was attributed to the polymer layer p(NIPAM-co-MAA) on the silica surface acting as a pH/temperature-dependent responsive polymer, which resulted in providing control release of loaded DOX after laser exposition in comparison with AuNR@DOX-MS and pure DOX, and consequently triggering

release at the appropriate time and location [79]. As a result of these findings, it was proven that the AuNR@DOX-MS@p(NIPAM-co-MAA) nanocomposite is a safe synergetic chemo-photothermal therapy, as it exhibits selective suppression of cancer cells efficiently after laser irradiation while having great safety on the viability of healthy cells MCF-10A.

In addition, flow cytometry was performed to detect MDA-MB-231cell apoptosis in each of the groups to further confirm the biosafety of synthesized AuNR@DOX-MS@p(NIPAM-co-MAA). As demonstrated by the results (Fig. 3B), cell apoptosis was significantly associated with AuNR@DOX-MS@p(NIPAM-co-MAA)+Laser. Moreover, as presented in Fig. 3C, the laser induction group of the synthesized AuNR@DOX-MS@p(NIPAM-co-MAA) nanocomposite possessed the highest number of apoptotic cells by around (52 ± 1%), as compared to the AuNR@DOX-MS + Laser (36.5 ± 1.3%), AuNR@DOX-MS-Laser (27.8 ± 1.2%), and the pure DOX groups (19 ± 2%). Meanwhile, pure nanomaterial groups, no matter without (6.9 ± 0.7%) or with (10.9 ± 0.3%) laser stimulation do not induce cell apoptosis, the AuNR@DOX-MS@p(NIPAM-co-MAA) (14.6 ± 0.6%) nanocomposite without laser irradiation revealed the lowest apoptotic cells, demonstrating that it has the ability to successfully prevent premature drug release and, as a result, has no adverse effects on healthy cells while having an efficient therapeutic effect on cancer cells.

3.4. Cellular uptake of synthesized AuNR@MS@DOX@p(NIPAM-co-MAA)

The uptake of AuNR@DOX-MS@p(NIPAM-co-MAA) and AuNR@DOX-MS in healthy cell line (MCF 10A) and cancer cell line (MDA-MB-231) was examined using flow cytometry at 2 h and 4 h' time points as shown in Fig. 4A and B, respectively. Cancer cells, particularly breast cancer cells, have a greater ability to migrate and metastasize and more easily endocytosis endogenous stimuli [80], so the uptake efficiency in the tumor cell line is higher during the specific co-incubator time than in the MCF-10A cell line. In addition, the AuNR@DOX-MS@p(NIPAM-co-MAA) was more likely to reach the uptake equilibrium in a short time when measuring the cellular uptake efficiency within 4 h *in vitro,* compared with the AuNR@DOX-MS group (Fig. 4C). p(NIPAM-co-MAA) can not only protect the loaded drug from premature release into the blood circulation but also further improve the biocompatibility of MS shells. Many studies have shown that mesoporous silica nanoparticles (MSN) coated with p(NIPAM-co-MAA) can reduce plasma protein adsorption to the MSN surface, as well as reduce the surface charge, and increase hydrophilicity [81,82]. However, it was observed that the cellular uptake of AuNR@DOX-MS increased during a 4-h incubation period, but AuNR@DOX-MS@p(NIPAM-co MAA) nanocomposite is seemed to reach its peak at 2 h (Fig. 4C). This was attributed to the fact that the produced nanocomposite was taken up more quickly and more efficiently by the cancer cells. Accordingly, the synthesized nanocomposite has the ability to reduce adverse effects in healthy cells while showing high uptake efficiency exclusively in cancer cells [32].

3.5. Biodistribution and photothermal efficacy of nanocomposite in vivo

To evaluate the thermoresponsive properties of fabricated nanocomposite AuNR@DOX-MS@p(NIPAM-co-MAA) *in vivo,* AuNR@DOX-MS@p(NIPAM-co-MAA) and PBS as a control group were injected intravenously into mice-bearing tumors, and an IR thermal camera was used to record changes in tumor temperature at specific time intervals. As revealed in Fig. 5A, a rapid increase in tumor temperature and higher fluorescence signal with the AuNR@DOX-MS@p(NIPAM-co-MAA) nanocomposite group were observed compared with the PBS group. Furthermore, while the tumor temperature in PBS was only increased by 5° from 32°C as a room temperature, which is less than 40°C, the tumor temperature in AuNR@DOX-MS@p(NIPAM-co-MAA) treated group reached up to 50°C after 2 min of irradiation with NIR laser (808 nm, 1 W cm^{-2}), which is sufficient to kill cancer cells effectively (Fig. 5B) [39]. This is an outcome of the accumulation of a high number of nanocomposites in the tumor region.

The targeted delivery of fabricated nanocomposite AuNR@DOX-MS@p(NIPAM-co-MAA) and its biodistribution in different body organs (heart, liver, spleen, lung, kidney, and tumor) was studied *in vivo* by fluorescence imaging experiments (Fig. 5C and D). AuNR@DOX-MS@p(NIPAM-co-MAA) and DOX alone were injected intravenously into mice-bearing tumors. The tissue of organs was collected and studied by ICP-MS analysis at 3 days post administration. As illustrated in Fig. 5C, the fluorescence signal of AuNR@DOX-MS@p(NIPAM-co-MAA) nanocomposite was much stronger than that of free DOX. In addition, with or without laser irradiation, AuNR@DOX-MS@p(NIPAM-co-MAA) accumulates more at the tumor site than free DOX (Fig. 5D) [32]. This is ascribed to the deposition of a polymer layer at the surface of the nanocomposite and hence reducing the opsonization of particles by blood proteins and phagocytosis of particles by macrophages. This further confirmed that the efficient tumor chemo-photothermal therapy of fabricated nanocomposite with minimized side effects.

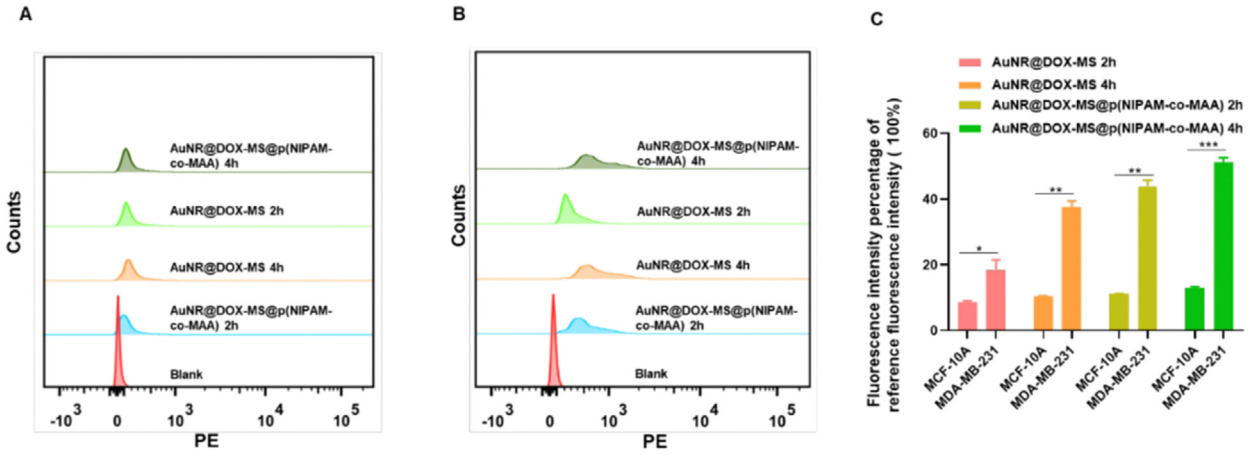

Fig. 4. (A) and (B) flow cytometry analysis of MCF-10A and MDA-MB-231cell line respectively after treatment with AuNR@DOX-MS and nanocomposite (AuNR@DOX-MSp(NIPAM-co-MAA)) for 2 h and 4 h. (C) Statistical analysis of MCF-10A and MDA-MB-231cells uptake after treatment with AuNR@DOX-MS, and AuNR@DOX-MS@p(NIPAM-co-MAA) for 2 h and 4 h (n = 3, *P <0.05, **P <0.01, and ***P <0.001).

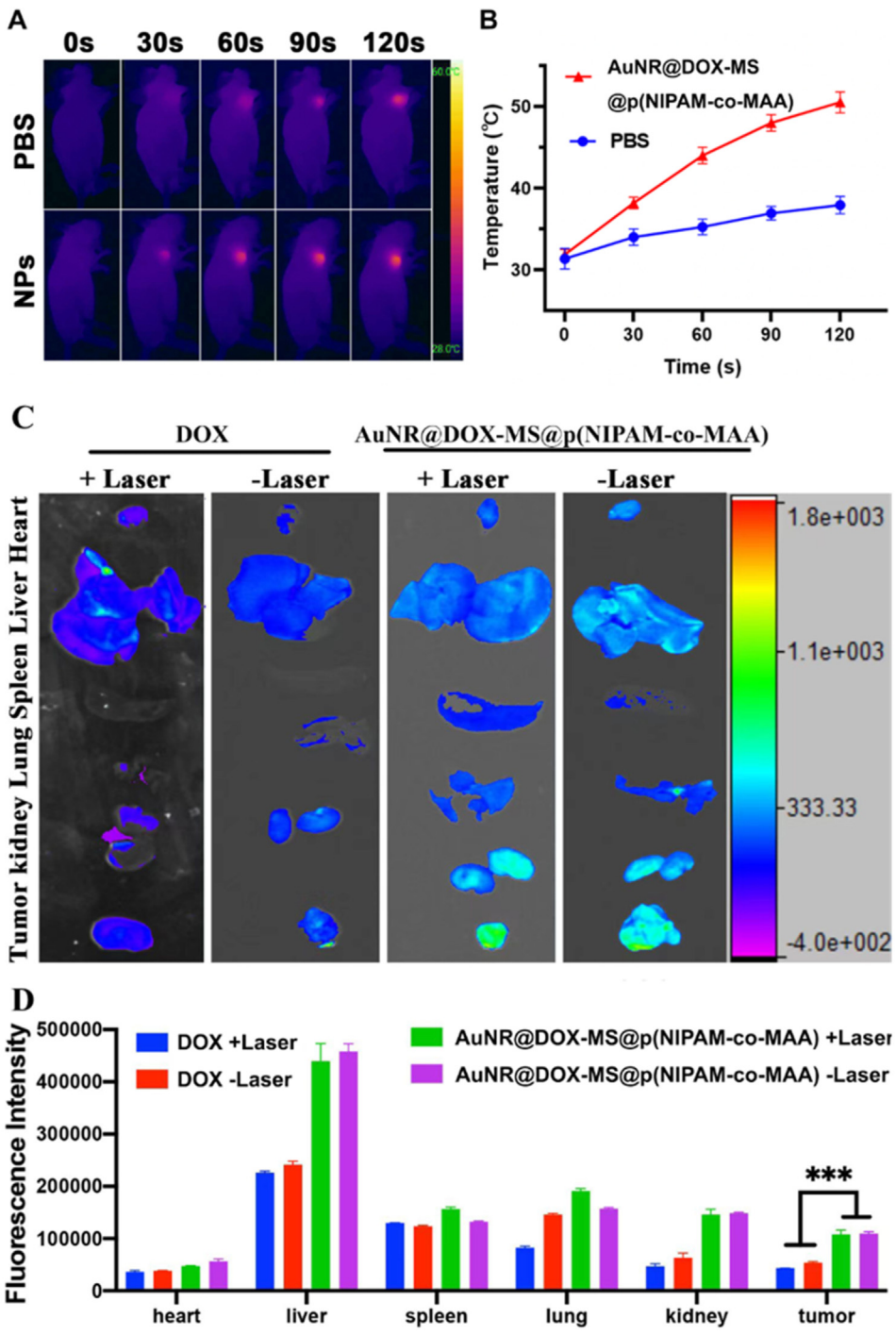

Fig. 5. Thermal imaging images of tumor-bearing mice, as well as images showing DOX and AuNR@DOX-MS@p(NIPAM-co-MAA) biodistribution *in vivo* and *in vitro*. (A) Infrared thermal images of the tumor-bearing mice taken at various time intervals while the tumor was continuously treated with a laser (808 nm, 1 W cm^{-2}) for 2 min. (B) time–temperature curve of tumors from mice following peritumoral PBS, and nanocomposite (AuNR@DOX-MS@p(NIPAM-co-MAA)) injection. (C) Near infrared fluorescence (NIRF) imaging of DOX fluorescence *in vitro*. (D) statistical analysis of fluorescence intensity of DOX in different organs and tumor (n = 3, ***P <0.001).

3.6. Anti-tumor activity and biosafety of AuNR@DOX-MS@p(NIPAM-co-MAA)

Moreover, to assess the chemo-photothermal efficacy of the fabricated nanocomposite as an anti-cancer delivery system, AuNR@DOX-MS@p(NIPAM-co-MAA), DOX, and PBS as control were injected intravenously into mice-bearing tumors after tumor volume exceeded 100 mm^3 (Fig. 6). According to tumor extracted photo and tumor volume (Fig. 6A and B), AuNR@DOX-MS@p(NIPAM-co-MAA) +Laser has a much higher efficacy than other groups, resulting in an 8-fold decrease in tumor volume compared to the PBS group. The final tumor volume of the PBS group was 362 mm^3, while it had dropped to around 44 mm^3 with AuNR@DOX-MS@p(NIPAM-co-MAA) +Laser at the end of the experiment. Likewise, as exhibited in Fig. 6C, the laser irradiation group of AuNR@DOX-MS@p(NIPAM-co-MAA) had the lowest tumor weight when compared to other groups, including DOX, PBS, and AuNR@DOX-MS@p(NIPAM-co-MAA)-Laser [39,41]. All the results suggest that the fabricated nanocomposite can effectively deliver synergistic chem-photothermal therapy to inhibit tumor growth.

Systemic safety evaluation of constructed nanocomposite AuNR@DOX-MS@p(NIPAM-co-MAA) was performed by monitoring the body weight and different organs (heart, liver, spleen, lung, and kidney) H & E staining pictures of the mice. As shown in Fig. 6D, there was a statistically significant variation in the body weight of tumor bearing mice between pure DOX and other different groups, including PBS, AuNR@DOX-MS@p(NIPAM-co-MAA)+Laser, and AuNR@DOX-MS@p(NIPAM-co-MAA)-Laser.

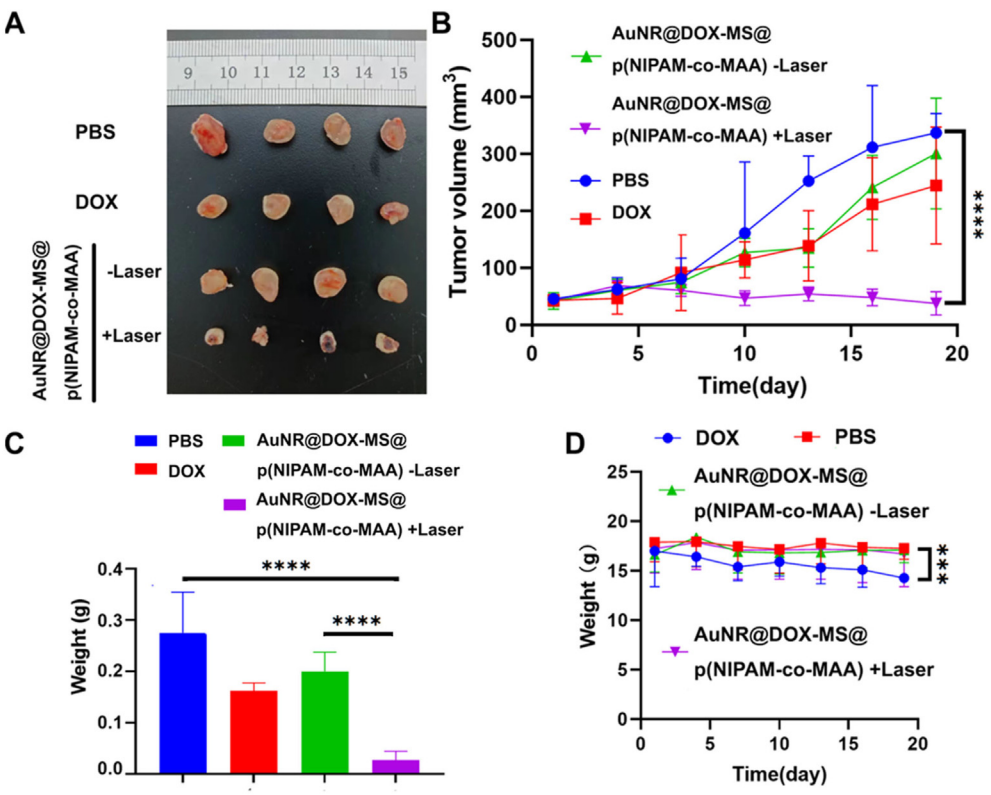

Fig. 6. Tumor treatment following intravenous adminstration of PBS, DOX, AuNR@DOX-MS@p(NIPAM-co-MAA)-Laser, and AuNR@DOX-MS@p(NIPAM-co-MAA)+ Laser. (A) A schematic representation of the experimental design, as well as the tumor photographs that were extracted following the therapy. (B) Changes in tumor volume during the 20-days treatment period. (C) Total weight of the tumors were removed.(D) Changes in the body weight of mice occur during the 15-day treatment period. (n = 4, ***P <0.001, and ****P <0.0001).

The pure DOX resulted in a considerable decrease in the body weight of mice, whereas there was no difference found in the body weight of mice treated with the laser induction group of fabricated nanocomposite or without laser in the same way as the PBS control group. In addition, H & E staining pictures of different groups showed that pure DOX severely damaged heart muscles, while the synthesized nanocomposite exhibited good biosafety and no obvious toxicity was detected in the various organs (liver, Spleen, lung, and kidney) (Supplementary Material Fig. S5). However, treatment with the constructed nanocomposite AuNR@DOX-MS@p(NIPAM-co-MAA) +Laser resulted in significant damage to cancer cell nuclei, whereas tumor tissues appeared very intact when treated with other groups (Fig S5). These results demonstrate that the fabricated nanocomposite AuNR@DOX-MS@p(NIPAM-co-MAA) is capable of providing effective tumor chemo-photothermal therapy while being biocompatible in healthy tissues when compared to pure DOX.

4. Conclusions

In summary, a nanocomposite was successfully constructed to have combined chemo-photothermal therapy capability with the aid of a pH/thermo-responsive polymer via encapsulating a silica-coated gold nanorod loaded with DOX in poly[(N-isopropylacrylamide)-co-(methacrylic acid) (AuNR@DOX-MS@p(NIPAM-co-MAA)). The AuNR induced hyperthermia in response to NIR radiation, while the silica shell functioned as a carrier for DOX delivery, and the polymer acted as a gatekeeper to control the DOX release. The synthesized nanocomposite prevented DOX from being released prematurely and accelerated its release in response to NIR radiation and pH condition at the tumor site, hence enhancing delivery of DOX into the tumor site. Additionally, the manufactured nanocomposite demonstrated effective tumor cell uptake and synergistic antitumor activity at the cellular level. *In vivo*, the generated nanocomposite had effective antitumor efficacy with good biodistribution to the tumor site. The constructed nanocomposite was found to have a high degree of biocompatibility with various organs. Thus, the synthesized chemo-photothermal treatment nanocomposite demonstrated synergistic efficacy *in vitro* and *in vivo* while maintaining a high level of biosafety and providing an enhanced and controllable release mechanism.

CRediT authorship contribution statement

Rawand A. Mustafa: Data curation, Formal analysis, Writing – original draft, Writing – review & editing. **Meixin Ran:** Data curation, Formal analysis. **Yonghui Wang:** Data curation, Formal analysis. **Jessica M. Rosenholm:** Supervision, Writing – review & editing. **Hongbo Zhang:** Supervision, Project administration, Writing – review & editing, Funding acquisition.

Declaration of competing interest

Authors declare no conflicts of interests. The authors declare that they have no known competing financial interests or personal relationships that could have appeared to influence the work reported in this paper.

Acknowledgments

Transmission electron microscopy (JEM-1400 Plus) imaging facility was provided by the Laboratory of Electron Microscopy, University of Turku, Finland. Imaging and flow cytometry were carried out at the Turku Bioscience Centre's Cell Imaging and Cytometry core, which is supported by Biocenter Finland. This work was supported by the National Natural Science Foundation of China (81871472), Research Fellow (Grant No. 328933), Solutions for Health Profile (336355), and In-FLAMES Flagship (337531) projects from Academy of Finland; as well as the Finland China Food and Health International Pilot Project funded by the Finnish Ministry of Education and Culture. Meixin Ran, Yonghui Wang and Jiaqi Yan was sponsored by the China Scholarship Council.

Appendix A. Supplementary data

Supplementary data to this article can be found online at https://doi.org/10.1016/j.smaim.2022.09.004.

References

[1] Y.S. Loo, N.I. Zahid, T. Madheswaran, I.D. Mat Azmi, Recent advances in the development of multifunctional lipid-based nanoparticles for co-delivery, combination treatment strategies, and theranostics in breast and lung cancer, J. Drug Deliv. Sci. Technol. 71 (2022), 103300.

[2] M. Zain, H. Yasmeen, S.S. Yadav, S. Amir, M. Bilal, A. Shahid, M. Khurshid, Chapter 10 - applications of nanotechnology in biological systems and medicine, in: A. Denizli, T.A. Nguyen, M. Rajan, M.F. Alam, K. Rahman (Eds.), Nanotechnology for Hematology, Blood Transfusion, and Artificial Blood, Elsevier, 2022, pp. 215–235.

[3] R. Gupta, H. Chauhan, V.K. Garg, N. Kataria, Chapter 9 - chemical and physical properties of nanoparticles and hybrid materials, in: J.R. Koduru, R.R. Karri, N.M. Mubarak, E.R. Bandala (Eds.), Sustainable Nanotechnology for Environmental Remediation, Elsevier, 2022, pp. 199–220.

[4] G. Liu, Q. Li, W. Ni, N. Zhang, X. Zheng, Y. Wang, D. Shao, G. Tai, Cytotoxicity of various types of gold-mesoporous silica nanoparticles in human breast cancer cells, Int. J. Nanomed. 10 (2015) 6075–6087.

[5] Z. Zhang, L. Wang, J. Wang, X. Jiang, X. Li, Z. Hu, Y. Ji, X. Wu, C. Chen, Mesoporous silica-coated gold nanorods as a light-mediated multifunctional theranostic platform for cancer treatment, Adv. Mater. 24 (2012) 1418–1423.

[6] X. Sun, J. Wang, Z. Wang, C. Zhu, J. Xi, L. Fan, J. Han, R. Guo, Gold nanorod@void@polypyrrole yolk@shell nanostructures: synchronous regulation of photothermal and drug delivery performance for synergistic cancer therapy, J. Colloid Interface Sci. 610 (2022) 89–97.

[7] D. Cheng, Y. Ji, B. Wang, Y. Wang, Y. Tang, Y. Fu, Y. Xu, X. Qian, W. Zhu, Dual-responsive nanohybrid based on degradable silica-coated gold nanorods for triple-combination therapy for breast cancer, Acta Biomater. 128 (2021) 435–446.

[8] L. Jiang, D. Chen, Z. Jin, C. Xia, Q. Xu, M. Fan, Y. Dai, J. Liu, Y. Li, Q. He, Light-triggered nitric oxide release and structure transformation of peptide for enhanced intratumoral retention and sensitized photodynamic therapy, Bioact. Mater. 12 (2022) 303–313.

[9] S.-h. Huang, S. Peng, Q.-y. Wang, Q.-h. Hu, R.-q. Zhang, L. Liu, Q. Liu, J. Lin, Q.-h. Zhou, Gold nanorods conjugated with biocompatible zwitterionic polypeptide for combined chemo-photothermal therapy of cervical cancer, Colloids Surf. B Biointerfaces 207 (2021), 112014.

[10] H. Chen, P. Timashev, Y. Zhang, X. Xue, X.J. Liang, Nanotechnology-based combinatorial phototherapy for enhanced cancer treatment, RSC Adv. 12 (2022) 9725–9737.

[11] M.R.K. Ali, Y. Wu, Y. Tang, H. Xiao, K. Chen, T. Han, N. Fang, R. Wu, M.A. El-Sayed, Targeting cancer cell integrins using gold nanorods in photothermal therapy inhibits migration through affecting cytoskeletal proteins, Proc. Natl. Acad. Sci. USA 114 (2017) E5655–E5663.

[12] J. Lee, Y.H. Lee, C.B. Jeong, J.S. Choi, K.S. Chang, M. Yoon, Gold nanorods-conjugated TiO2 nanoclusters for the synergistic combination of phototherapeutic treatments of cancer cells, J. Nanobiotechnol. 16 (2018) 104.

[13] P. Singh, Y.J. Kim, H. Singh, S. Ahn, V. Castro-Aceituno, D.C. Yang, In situ preparation of water-soluble ginsenoside Rh2-entrapped bovine serum albumin nanoparticles: in vitro cytocompatibility studies, Int. J. Nanomed. 12 (2017) 4073–4084.

[14] X. Wang, T. Xiong, M. Cui, N. Li, Q. Li, L. Zhu, S. Duan, Y. Wang, Y. Guo, A novel targeted co-delivery nanosystem for enhanced ovarian cancer treatment via multidrug resistance reversion and mTOR-mediated signaling pathway, J. Nanobiotechnol. 19 (2021) 444.

[15] J. Chen, X. Li, X. Zhao, Q. Wu, H. Zhu, Z. Mao, C. Gao, Doxorubicin-conjugated pH-responsive gold nanorods for combined photothermal therapy and chemotherapy of cancer, Bioact. Mater. 3 (2018) 347–354.

[16] J. Li, N. Yang, M. Yang, C. Lu, M. Xie, Development of a magnetic MoS2 system camouflaged by lipid for chemo/phototherapy of cancer, Colloids Surf. B Biointerfaces 213 (2022), 112389.

[17] X. Jin, S. Yao, F. Qiu, Z. Mao, B. Wang, A multifunctional hydrogel containing gold nanorods and methylene blue for synergistic cancer phototherapy, Colloids Surf. A Physicochem. Eng. Asp. 614 (2021), 126154.

[18] C. Qin, J. Fei, A. Wang, Y. Yang, J. Li, Rational assembly of a biointerfaced core@shell nanocomplex towards selective and highly efficient synergistic photothermal/photodynamic therapy, Nanoscale 7 (2015) 20197–20210.

[19] J. Yang, X. Zhang, C. Liu, Z. Wang, L. Deng, C. Feng, W. Tao, X. Xu, W. Cui, Biologically modified nanoparticles as theranostic bionanomaterials, Prog. Mater. Sci. 118 (2021), 100768.

[20] Y. Cao, Q. Ren, R. Hao, Z. Sun, Innovative strategies to boost photothermal therapy at mild temperature mediated by functional nanomaterials, Mater. Des. 214 (2022), 110391.

[21] S. Li, Y. Wu, X. Xue, S. Liu, NIR and reduction dual-sensitive polymeric prodrug nanoparticles for bioimaging and combined chemo-phototherapy, Polymers 14 (2) (2022) 287.

[22] X. Cui, W. Cheng, X. Han, Lipid bilayer modified gold nanorod@mesoporous silica nanoparticles for controlled drug delivery triggered by near-infrared light, J. Mater. Chem. B 6 (2018) 8078–8084.

[23] D. Rohleder, P. Vana, Near-infrared-triggered photothermal aggregation of polymer-grafted gold nanorods in a simulated blood fluid, Biomacromolecules 22 (2021) 1614–1624.

[24] T.A. Jacinto, C.F. Rodrigues, A.F. Moreira, S.P. Miguel, E.C. Costa, P. Ferreira, I.J. Correia, Hyaluronic acid and vitamin E polyethylene glycol succinate functionalized gold-core silica shell nanorods for cancer targeted photothermal therapy, Colloids Surf. B Biointerfaces 188 (2020), 110778.

[25] W. Zeng, X. Wu, T. Chen, S. Sun, Z. Shi, J. Liu, X. Ji, X. Zeng, J. Guan, L. Mei, M. Wu, Renal-clearable ultrasmall polypyrrole nanoparticles with size-regulated property for second near-infrared light-mediated photothermal therapy, Adv. Funct. Mater. 31 (2021), 2008362.

[26] L. Fan, X. Zhang, M. Nie, Y. Xu, Y. Wang, L. Shang, Y. Zhao, Y. Zhao, Photothermal responsive microspheres-triggered separable microneedles for versatile drug delivery, Adv. Funct. Mater. 32 (2022), 2110746.

[27] J. Choi, S.Y. Kim, Photothermally enhanced photodynamic therapy based on glutathione-responsive pheophorbide a-conjugated gold nanorod formulations for cancer theranostic applications, J. Ind. Eng. Chem. 85 (2020) 66–74.

[28] J.H. Park, K.E. Sung, K.H. Kim, J.R. Kim, J. Kim, G.D. Moon, D.C. Hyun, Dual gate-keeping and reversible on-off switching drug release for anti-cancer therapy with pH- and NIR light-responsive mesoporous silica-coated gold nanorods, J. Ind. Eng. Chem. 106 (2022) 233–242.

[29] J.K.K. Cheong, V. Popov, E. Alchera, I. Locatelli, M. Alfano, L. Menichetti, P. Armanetti, M. Maturi, M.C. Franchini, E.H. Ooi, Y.S. Chiew, A numerical study to investigate the effects of tumour position on the treatment of bladder cancer in mice using gold nanorods assisted photothermal ablation, Comput. Biol. Med. 138 (2021), 104881.

[30] X. Ye, L. Jin, H. Caglayan, J. Chen, G. Xing, C. Zheng, V. Doan-Nguyen, Y. Kang, N. Engheta, C.R. Kagan, C.B. Murray, Improved size-tunable synthesis of monodisperse gold nanorods through the use of aromatic additives, ACS Nano 6 (2012) 2804–2817.

[31] D. Shajari, A. Bahari, P. Gill, M. Mohseni, Synthesis and tuning of gold nanorods with surface plasmon resonance, Opt. Mater. 64 (2017) 376–383.

[32] B. Gong, Y. Shen, H. Li, X. Li, X. Huan, J. Zhou, Y. Chen, J. Wu, W. Li, Thermo-responsive polymer encapsulated gold nanorods for single continuous wave laser-induced photodynamic/photothermal tumour therapy, J. Nanobiotechnol. 19 (2021) 41.

[33] X. Gu, V. Timchenko, G. Heng Yeoh, L. Dombrovsky, R. Taylor, The effect of gold nanorods clustering on near-infrared radiation absorption, Appl. Sci. 8 (7) (2018).

[34] X. Kang, X. Guo, X. Niu, W. An, S. Li, Z. Liu, Y. Yang, N. Wang, Q. Jiang, C. Yan, H. Wang, Q. Zhang, Photothermal therapeutic application of gold nanorods-porphyrin-trastuzumab complexes in HER2-positive breast cancer, Sci. Rep. 7 (2017), 42069.

[35] S.-H. Seo, B.-M. Kim, A. Joe, H.-W. Han, X. Chen, Z. Cheng, E.-S. Jang, NIR-light-induced surface-enhanced Raman scattering for detection and photothermal/photodynamic therapy of cancer cells using methylene blue-embedded gold nanorod@SiO2 nanocomposites, Biomaterials 35 (2014) 3309–3318.

[36] J. Kadkhoda, A. Tarighatnia, J. Barar, A. Aghanejad, S. Davaran, Recent advances and trends in nanoparticles based photothermal and photodynamic therapy, Photodiagnosis Photodyn. Ther. 37 (2022), 102697.

[37] J. Liu, C. Detrembleur, M.-C. De Pauw-Gillet, S. Mornet, C. Jérôme, E. Duguet, Gold nanorods coated with mesoporous silica shell as drug delivery system for remote near infrared light-activated release and potential phototherapy, Small 11 (2015) 2323–2332.

[38] H. Yang, M. Xu, S. Li, X. Shen, T. Li, J. Yan, C. Zhang, C. Wu, H. Zeng, Y. Liu, Chitosan hybrid nanoparticles as a theranostic platform for targeted doxorubicin/VEGF shRNA co-delivery and dual-modality fluorescence imaging, RSC Adv. 6 (2016) 29685–29696.

[39] Z. Zhang, J. Wang, X. Nie, T. Wen, Y. Ji, X. Wu, Y. Zhao, C. Chen, Near infrared laser-induced targeted cancer therapy using thermoresponsive polymer encapsulated gold nanorods, J. Am. Chem. Soc. 136 (2014) 7317–7326.

[40] G. Li, Y. Chen, L. Zhang, M. Zhang, S. Li, L. Li, T. Wang, C. Wang, Facile approach to synthesize gold Nanorod@Polyacrylic acid/calcium phosphate yolk–shell nanoparticles for dual-mode imaging and pH/NIR-responsive drug delivery, Nano-Micro Lett. 10 (2017) 7.

[41] N.T. Ha Lien, A.D. Phan, B.T. Van Khanh, N.T. Thuy, N. Trong Nghia, H.T. My Nhung, T. Hong Nhung, D. Quang Hoa, V. Duong, N. Minh Hue, Applications of mesoporous silica-encapsulated gold nanorods loaded doxorubicin in chemo-photothermal therapy, ACS Omega 5 (2020) 20231–20237.

[42] J. Feng, Z. Wang, B. Shen, L. Zhang, X. Yang, N. He, Effects of template removal on both morphology of mesoporous silica-coated gold nanorod and its biomedical application, RSC Adv. 4 (2014) 28683–28690.

[43] C. Wu, Q.-H. Xu, Stable and functionable mesoporous silica-coated gold nanorods as sensitive localized surface plasmon resonance (LSPR) nanosensors, Langmuir 25 (2009) 9441–9446.

[44] Y.H. Roh, J.Y. Eom, D.G. Choi, J.Y. Moon, M.S. Shim, K.W. Bong, Gold nanorods-encapsulated thermosensitive drug carriers for NIR light-responsive anticancer therapy, J. Ind. Eng. Chem. 98 (2021) 211–216.

[45] S.H. Lee, M.K. Gupta, J.B. Bang, H. Bae, H.-J. Sung, Current progress in reactive oxygen species (ROS)-Responsive materials for biomedical applications, Advanced Healthcare Materials 2 (2013) 908–915.

[46] S. Ganta, H. Devalapally, A. Shahiwala, M. Amiji, A review of stimuli-responsive nanocarriers for drug and gene delivery, J. Contr. Release 126 (2008) 187–204.

[47] F. Meng, Z. Zhong, J. Feijen, Stimuli-responsive polymersomes for programmed drug delivery, Biomacromolecules 10 (2009) 197–209.

[48] N. Rapoport, Physical stimuli-responsive polymeric micelles for anti-cancer drug delivery, Prog. Polym. Sci. 32 (2007) 962–990.

[49] K. Li, X. Zang, M. Cheng, X. Chen, Stimuli-responsive nanoparticles based on poly acrylic derivatives for tumor therapy, Int. J. Pharm. 601 (2021), 120506.
[50] O. Veiseh, J.W. Gunn, M. Zhang, Design and fabrication of magnetic nanoparticles for targeted drug delivery and imaging, Adv. Drug Deliv. Rev. 62 (2010) 284–304.
[51] A. Schroeder, J. Kost, Y. Barenholz, Ultrasound, liposomes, and drug delivery: principles for using ultrasound to control the release of drugs from liposomes, Chem. Phys. Lipids 162 (2009) 1–16.
[52] A.S. Monem, N. Elbialy, N. Mohamed, Mesoporous silica coated gold nanorods loaded doxorubicin for combined chemo–photothermal therapy, Int. J. Pharm. 470 (2014) 1–7.
[53] R. Salehi, S. Rasouli, H. Hamishehkar, Smart thermo/pH responsive magnetic nanogels for the simultaneous delivery of doxorubicin and methotrexate, Int. J. Pharm. 487 (2015) 274–284.
[54] S. Porrang, N. Rahemi, S. Davaran, M. Mahdavi, B. Hassanzadeh, Synthesis of temperature/pH dual-responsive mesoporous silica nanoparticles by surface modification and radical polymerization for anti-cancer drug delivery, Colloids Surf. A Physicochem. Eng. Asp. 623 (2021), 126719.
[55] G. Li, I. Varga, A. Kardos, I. Dobryden, P.M. Claesson, Temperature-dependent nanomechanical properties of adsorbed poly-NIPAm microgel particles immersed in water, Langmuir 37 (2021) 1902–1912.
[56] H. Tomonaga, Y. Tanigaki, K. Hayashi, T. Matsuyama, J. Ida, Adsorption properties of poly(NIPAM-co-AA) immobilized on silica-coated magnetite nanoparticles prepared with different acrylic acid content for various heavy metal ions, Chem. Eng. Res. Des. 171 (2021) 213–224.
[57] H. Wei, S.-X. Cheng, X.-Z. Zhang, R.-X. Zhuo, Thermo-sensitive polymeric micelles based on poly(N-isopropylacrylamide) as drug carriers, Prog. Polym. Sci. 34 (2009) 893–910.
[58] Z.H. Farooqi, H.U. Khan, S.M. Shah, M. Siddiq, Stability of poly(N-isopropylacrylamide-co-acrylic acid) polymer microgels under various conditions of temperature, pH and salt concentration, Arab. J. Chem. 10 (2017) 329–335.
[59] C. Cheng, H. Wei, B.-X. Shi, H. Cheng, C. Li, Z.-W. Gu, S.-X. Cheng, X.-Z. Zhang, R.-X. Zhuo, Biotinylated thermoresponsive micelle self-assembled from double-hydrophilic block copolymer for drug delivery and tumor target, Biomaterials 29 (2008) 497–505.
[60] M.L. Ohnsorg, J.M. Ting, S.D. Jones, S. Jung, F.S. Bates, T.M. Reineke, Tuning PNIPAm self-assembly and thermoresponse: roles of hydrophobic end-groups and hydrophilic comonomer, Polym. Chem. 10 (2019) 3469–3479.
[61] J. He, L. Tremblay, S. Lacelle, Y. Zhao, How can photoisomerization of azobenzene induce a large cloud point temperature shift of PNIPAM? Polym. Chem. 5 (2014) 5403–5411.
[62] E. Djokpé, W. Vogt, N-isopropylacrylamide and N-Isopropylmethacryl-amide: cloud points of mixtures and copolymers, Macromol. Chem. Phys. 202 (2001) 750–757.
[63] X. Jin, Q. Wang, J. Sun, H. Panezail, X. Wu, S. Bai, Dual temperature- and pH-responsive ibuprofen delivery from poly(N-isopropylacrylamide-co-acrylic acid) nanoparticles and their fractal features, Polym. Bull. 74 (2017) 3619–3638.
[64] X. Liu, D. Yu, C. Jin, X. Song, J. Cheng, X. Zhao, X. Qi, G. Zhang, A dual responsive targeted drug delivery system based on smart polymer coated mesoporous silica for laryngeal carcinoma treatment, New J. Chem. 38 (2014) 4830–4836.
[65] R. Zhao, X. Han, Y. Li, H. Wang, T. Ji, Y. Zhao, G. Nie, Photothermal effect enhanced cascade-targeting strategy for improved pancreatic cancer therapy by gold Nanoshell@Mesoporous silica nanorod, ACS Nano 11 (2017) 8103–8113.
[66] L. Scarabelli, A. Sánchez-Iglesias, J. Pérez-Juste, L.M. Liz-Marzán, A "tips and tricks" practical guide to the synthesis of gold nanorods, J. Phys. Chem. Lett. 6 (2015) 4270–4279.
[67] X. Zhou, W. Feng, K. Qiu, L. Chen, W. Wang, W. Nie, X. Mo, C. He, BMP-2 derived peptide and dexamethasone incorporated mesoporous silica nanoparticles for enhanced osteogenic differentiation of bone mesenchymal stem cells, ACS Appl. Mater. Interfaces 7 (2015) 15777–15789.
[68] M. Hegazy, P. Zhou, G. Wu, L. Wang, N. Rahoui, N. Taloub, X. Huang, Y. Huang, Construction of polymer coated core–shell magnetic mesoporous silica nanoparticles with triple responsive drug delivery, Polym. Chem. 8 (2017) 5852–5864.
[69] F. Howaili, E. Özliseli, B. Küçüktürkmen, S.M. Razavi, M. Sadeghizadeh, J.M. Rosenholm, Stimuli-responsive, plasmonic nanogel for dual delivery of curcumin and photothermal therapy for cancer treatment, Front. Chem. 8 (2021).
[70] J. Yan, Y. Wang, M. Ran, R.A. Mustafa, H. Luo, J. Wang, J.-H. Smått, J.M. Rosenholm, W. Cui, Y. Lu, Z. Guan, H. Zhang, Peritumoral microgel reservoir for long-term light-controlled triple-synergistic treatment of osteosarcoma with single ultra-low dose, Small 17 (2021), 2100479.
[71] J. Yan, C. Liu, Q. Wu, J. Zhou, X. Xu, L. Zhang, D. Wang, F. Yang, H. Zhang, Mineralization of pH-sensitive doxorubicin prodrug in ZIF-8 to enable targeted delivery to solid tumors, Anal. Chem. 92 (2020) 11453–11461.
[72] S. Peretz Damari, D. Shamrakov, M. Varenik, E. Koren, E. Nativ-Roth, Y. Barenholz, O. Regev, Practical aspects in size and morphology characterization of drug-loaded nano-liposomes, Int. J. Pharm. 547 (2018) 648–655.
[73] S.K. Brar, M. Verma, Measurement of nanoparticles by light-scattering techniques, TrAC, Trends Anal. Chem. 30 (2011) 4–17.
[74] R. Bansal, R. Singh, K. Kaur, Quantitative analysis of doxorubicin hydrochloride and arterolane maleate by mid IR spectroscopy using transmission and reflectance modes, BMC Chemistry 15 (2021) 27.
[75] X. Li, C. Gao, Y. Wu, C.Y. Cheng, W. Xia, Z. Zhang, Combination delivery of Adjudin and Doxorubicin via integrating drug conjugation and nanocarrier approaches for the treatment of drug-resistant cancer cells, J. Mater. Chem. B 3 (2015) 1556–1564.
[76] B. Chang, X. Sha, J. Guo, Y. Jiao, C. Wang, W. Yang, Thermo and pH dual responsive, polymer shell coated, magnetic mesoporous silica nanoparticles for controlled drug release, J. Mater. Chem. 21 (2011) 9239–9247.
[77] Z.H. Farooqi, Z. Butt, R. Begum, S.R. Khan, A. Sharif, E. Ahmed, Poly(N-isopropylacrylamide-co-methacrylic acid) microgel stabilized copper nanoparticles for catalytic reduction of nitrobenzene, Mater. Sci.Poland 33 (2016) 627–634.
[78] L. Zhang, X. Ma, W. Zhou, Q. Wu, J. Yan, X. Xu, B. Ghimire, J.M. Rosenholm, J. Feng, D. Wang, H. Zhang, Combination of photothermal, prodrug and tumor cell camouflage technologies for triple-negative breast cancer treatment, Mater .Today .Adv 13 (2022), 100199.
[79] W. Xiong, W. Wang, Y. Wang, Y. Zhao, H. Chen, H. Xu, X. Yang, Dual temperature/pH-sensitive drug delivery of poly(N-isopropylacrylamide-co-acrylic acid) nanogels conjugated with doxorubicin for potential application in tumor hyperthermia therapy, Colloids Surf. B Biointerfaces 84 (2011) 447–453.
[80] O.J. Scully, B.-H. Bay, G. Yip, Y. Yu, Breast cancer metastasis, Cancer Genomics Proteomics 9 (2012) 311.
[81] Y. Chen, W. Yang, B. Chang, H. Hu, X. Fang, X. Sha, In vivo distribution and antitumor activity of doxorubicin-loaded N-isopropylacrylamide-co-methacrylic acid coated mesoporous silica nanoparticles and safety evaluation, Eur. J. Pharm. Biopharm. 85 (2013) 406–412.
[82] J.-C. Leroux, E. Roux, D. Le Garrec, K. Hong, D.C. Drummond, N-isopropylacrylamide copolymers for the preparation of pH-sensitive liposomes and polymeric micelles, J. Contr. Release 72 (2001) 71–84.